Electronic modulation induced by decorating single-atomic Fe-Co pairs with Fe-Co alloy clusters toward enhanced ORR/OER activity

Ping Li [a],[1], Fuqiang Qiang [a],[1], Xuehai Tan [b], Zhi Li [b],[*], Jing Shi [a], Shuai Liu [a], Minghua Huang [a], Jingwei Chen [a], Weiqian Tian [a], Jingyi Wu [a], Wei Hu [c],[*], Huanlei Wang [a],[*]

[a] School of Materials Science and Engineering, Ocean University of China, Qingdao 266404, China
[b] Department of Chemical and Materials Engineering, University of Alberta, Edmonton, Alberta T6G 2V4, Canada
[c] School of Chemistry and Chemical Engineering, Qilu University of Technology, Jinan 250353, China

ARTICLE INFO

ABSTRACT

Modulating the electronic properties of single-atomic metal sites with metal clusters is a promising strategy for boosting their intrinsic oxygen reduction reaction (ORR) and oxygen evolution reaction (OER) activity. Herein, we report an effective isolation-confinement strategy for synthesis of well-dispersed Fe-Co atom clusters and N_4Fe-CoN_4 atomic pair sites on carbon nanofibers (marked as β-FeCo-PCNF), in which the addition of β-cyclo-dextrin is crucial in avoiding the agglomeration of metal species. The Fe-Co atomic clusters induce a downward shift in the *d*-band center of Fe-Co atomic sites, and this shift effectively reduces the adsorption energy of OOH* on Fe-Co atomic sites, resulting in lower energy barriers for ORR and OER. Remarkably, the β-FeCo-PCNF-based Zn-air battery exhibits excellent power density and cycling stability. This work paves the way for a universal strategy to regulate the electronic localization of atomic pair sites by alloy clusters and provides essential guidance for designing multifunctional electrocatalysts.

1. Introduction

The development and utilization of novel energy storage and conversion devices to replace conventional fossil fuels is a crucial step towards achieving carbon neutrality [1,2]. Rechargeable Zn-air battery with the characteristics of high theoretical specific energy, cost-effectiveness, and environmental friendliness shows great potential in this field [3,4]. However, the main challenge facing Zn-air batteries is the high overpotential and poor stability resulting from sluggish kinetics of the oxygen reduction reaction (ORR) and oxygen evolution reaction (OER) [5]. Therefore, the key issue is to identify efficient bifunctional electrocatalysts that can significantly enhance the ORR and OER processes. While the current benchmark ORR/OER catalysts are made of precious metals [6–8], their large-scale commercial use is impeded by their high cost and poor stability [9,10]. Hence, it is highly desirable to develop catalysts that possess high-performance, superior stability, abundant resources, and low cost, such as transition metal-based bifunctional catalysts.

Among transition metal-based catalysts, single atom catalysts are widely studied due to their high atom utilization efficiency, remarkable catalytic activity, and superior reaction selectivity [11–13]. However, despite their promising results, their catalytic performance still requires further improvement [14]. Two main methods for achieving this are adding more active sites or increasing the intrinsic activity of existing active sites [15,16]. Increasing the number of active sites is beneficial but often leads to the agglomeration of metal atoms, reducing the atomic utilization [17]. Therefore, increasing the intrinsic activity of single atom sites becomes more essential [18]. Recent research has shown that the suboptimal intrinsic activity of active sites in single atom catalysts is related to the non-optimal adsorption/desorption of intermediates for ORR/OER [19]. Adjusting the electronic configuration of active metal central sites is a promising strategy to alter the adsorption/desorption of ORR/OER intermediates, thus improving catalytic performance [20]. The introduction of another metallic center can optimize the adsorption/desorption characteristics by changing the electron distribution of the metal sites, resulting in boosting the intrinsic catalytic activity of single atoms [21,22]. For example, Zhu et al.[23] and Zhong et al.[24] introduced Ni and Pt single-atom sites into the Fe single atom catalysts

for forming bimetallic single-atom catalysts, exhibiting better catalytic activity compared to single-metal catalysts. Additionally, the introduction of atomic clusters can also enhance the catalytic activity by inducing electron redistribution with the strong interaction between single-atomic sites and clusters [25]. Similarly, incorporating alloy clusters, such as FeCo clusters with superior OER catalytic activity [26, 27], into single atom catalysts is promising for simultaneously enhancing both the ORR and OER performance. However, due to the high competitiveness of single atoms and metal clusters during the preparation process, there are few reports on the decoration of clusters for promoting the intrinsic catalytic activity of single-atomic active sites [28].

Generally, as the size of metal particles decreases, the specific surface area dramatically increases, which in turn leads to a significant increase in the free energy of the metal surface. This increased energy can cause the metal sites to agglomerate and form larger particles. Porous materials with the confinement effect can act as the host to prepare single-atom/cluster catalysts, with a focus on size control, front tuning, and morphology modulation [29]. One of the typical porous materials is covalent organic frameworks (COFs) [30]. The metal ions can diffuse into the cavity of COFs, and the periodic structure with separated units of COFs can inhibit the clustering of metal atoms during pyrolysis [29]. However, the relatively complex synthesis process of COFs is not conducive to large-scale applications. Therefore, finding a readily available and cost-effective alternative strategy to COFs is desirable [31]. One such promising alternative is β-cyclodextrin (β-CD), a naturally occurring molecule composed of seven D-(+)-glucose units connected by 1,4-α-linkages. This molecule has a torus-shaped ring structure with an internal diameter ranging from 0.5 to 0.8 nm [32]. The cavity of β-CD enables the formation of host-guest inclusion complexes by binding molecules or metal ions, similar to the mechanism observed in COFs [33]. Thus, β-CD is expected to be a suitable replacement for COFs in the preparation of single-atom/cluster catalysts.

Herein, we propose a simple and efficient isolation-confinement method for synthesizing Fe-Co atomic pair sites and Fe-Co alloy clusters anchored onto porous carbon nanofibers (β-FeCo-PCNF) catalyst. In the preparation of β-FeCo-PCNF, the diffusion of metal ions into the cavities of the β-CD is a critical step in preventing metal agglomeration, and the introduction of β-CD also acts as a pore-forming agent, generating a large specific surface area for exposing rich active catalytic sites. Synchrotron X-ray absorption spectroscopy confirms the formation of N_4Fe-CoN_4 atomic pairs bonding to Fe-Co alloy clusters in β-FeCo-PCNF. The synergy between Fe-Co atomic pairs and Fe-Co clusters, combined with the high exposure of active sites, leads to the outstanding bifunctional catalytic activity in both ORR and OER for β-FeCo-PCNF. It has been found that the Fe-Co alloy clusters modulate the electron distribution of Fe-Co atomic sites so that the *d*-band center of Fe-Co atomic sites is negatively shifted, which significantly reduces the adsorption energy of the initially high OOH* and thus achieves a lower energy barrier of ORR and OER. Moreover, the β-FeCo-PCNF-based Zn-air battery also exhibits remarkable electrochemical performance.

2. Experimental section

2.1. Synthesis of β-FeCo-PCNF

0.17 g β-cyclodextrin (β-CD) was firstly dissolved into 10 mL DMF with stirring for 30 min at room temperature, and then 0.1 mmol Fe $(NO_3)_3 \cdot 9$ H_2O and 0.05 mmol Co$(NO_3)_2 \cdot 6$ H_2O were added with stirring for 2 h. Next, 0.5 g polyacrylonitrile (PAN) was added into the above solution and stirred overnight. Subsequently, the mixed solution was transferred into a plastic syringe equipped with a stainless-steel needle for the electrospinning process, in which the feed rate, applied voltage, and spin distance were 2 mL h^{-1}, 16 kV, and 16 cm. The as-spun nanofiber membranes were oxidized in tube furnace at 280 °C (2 °C min^{-1}) for 2 h in air, and then directly carbonized at 1000 °C (5 °C

min^{-1}) for 2 h under N_2 atmosphere to obtain β-FeCo-PCNF.

2.2. Synthesis of FeCo-CNF

FeCo-CNF was prepared via the same procedure for β-FeCo-PCNF without adding β-cyclodextrin.

2.3. Synthesis of β-Co-PCNF

The β-Co-PCNF was synthesized using the same method as β-FeCo-PCNF, and only Co$(NO_3)_2 \cdot 6$ H_2O (0.15 mmol) was added during the preparation process.

2.4. Synthesis of β-Fe-PCNF

The β-Fe-PCNF was synthesized using the same method as β-FeCo-PCNF, and only Fe$(NO_3)_3 \cdot 9$ H_2O (0.15 mmol) was added during the preparation process.

2.5. Synthesis of β-Fe-PCNF-AC

β-FeCo-PCNF-AC was prepared by washing the β-FeCo-PCNF sample with 2 M HCl at 90 ºC for 24 h to remove the FeCo clusters.

2.6. Synthesis of PCNF

The PCNF was prepared using the same method as β-FeCo-PCNF without the addition of metal salts and β-CD.

Details of Material characterization, electrochemical measurements, assembley of liquid Zn-air battery and computation methods are shown in supporting information.

3. Results and discussion

3.1. Synthesis and characterization of β-FeCo-PCNF catalyst.

The β-FeCo-PCNF catalyst was synthesized using a facile isolation-confinement strategy (Fig. 1). Initially, iron and cobalt ions were adsorbed and confined within the cavities of β-CD [34]. The addition of PAN then effectively isolated the metal-adsorbed β-CD to form a homogeneous solution. The above solution was electrostatically spun to obtain nanofibers due to the superior compatibility between metal-absorbed β-CD and PAN. Comparison of the pore size distributions of the as-spun nanofibers with and without metal salts revealed that pores smaller than 2 nm were completely blocked by the addition of metal salts (Fig. S1), providing evidence of the incorporation of metal ions into the cavities of β-CD. During the pyrolysis process, the metal salts confined in the β-CD cavity first decomposed into metal oxides, which then reacted with carbon to produce metal species [35]. The restricted space of β-CD facilitated diffusion of the metal to form a large number of Fe-Co atomic pair sites along with Fe-Co alloy clusters [36]. Simultaneously, the pore-forming function of β-CD and the corrosive effect of metal clusters on carbon led to nanofibers with a rich pore structure and a very large specific surface area [37], greatly facilitating the exposure of active sites and the transport of electrolyte.

The scanning electron microscopy (SEM) image of β-FeCo-PCNF (Fig. 2a) reveals a typical 3D network structure with randomly entangled fibers that are similar to those of our previously synthesized β-PCNF without metal addition[37]. This finding suggests that the confinement effect of β-CD on the metal precursor can maintain the fiber shape. The observed rough surface of β-FeCo-PCNF can be attributed to the emission of volatile gases during the decomposition of β-CD. It is worth noting that no obvious metal particles can be identified on the surface of β-FeCo-PCNF, indicating that severe agglomeration of metal atoms did not occur during the pyrolysis process. However, the FeCo-CNF synthesized without β-CD shows the morphology of stacks of short fibers
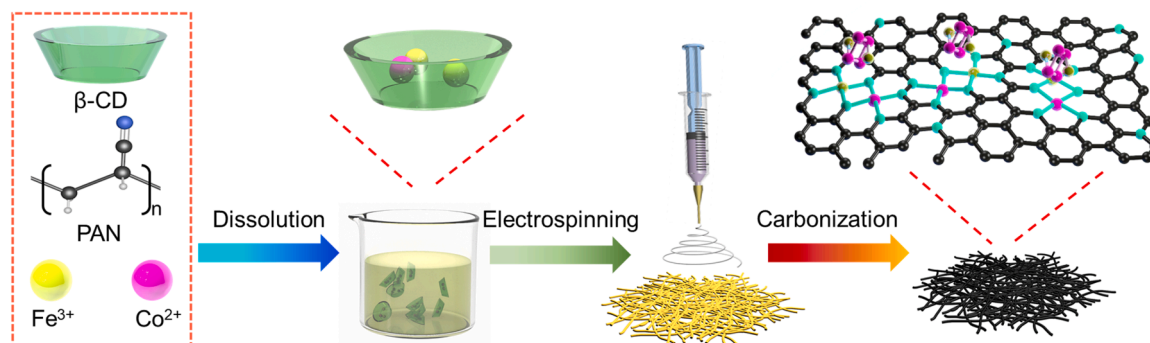
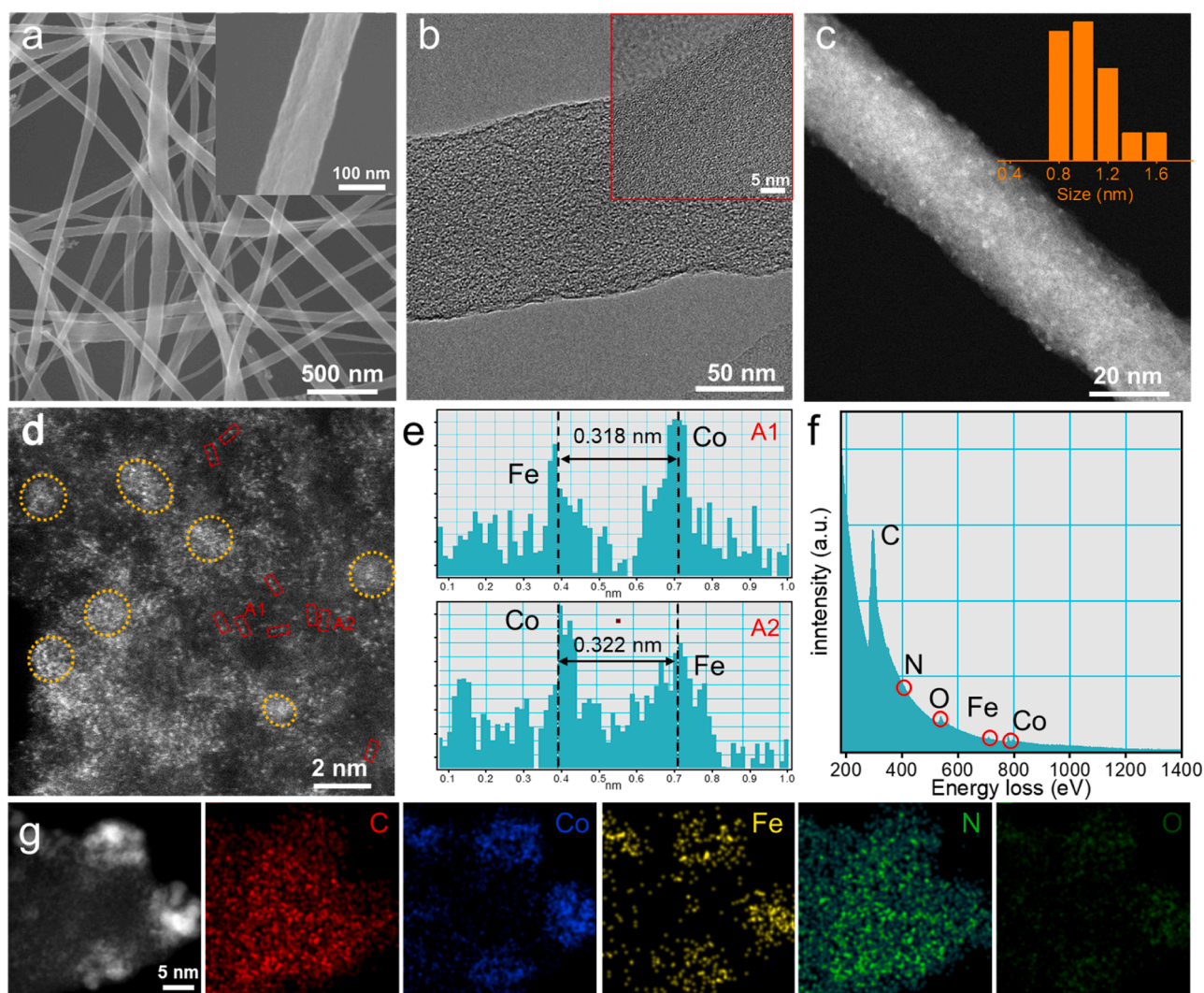**Fig. 1.** Schematic illustration of the synthesis of β-FeCo-PCNF.

Fig. 2. (a) SEM images of β-FeCo-PCNF. (b) TEM image of β-FeCo-PCNF. (c) HAADF-STEM image at low magnification and particle size distribution histogram (inset) of β-FeCo-PCNF. (d) Aberration-corrected HAADF-STEM image of β-FeCo-PCNF (Some of the Fe-Co dual atom sites are marked with red rectangles and some of Fe-Co alloy clusters are marked wirh yellow circles). (e) Intersity profiles of Fe-Co dual atom sites extracted from the areas of A1 and A2 in (d). (f) EELS atomic spectra of Fe, Co, C, N and O elements for β-FeCo-PCNF. (g) EDXS elemental mappings of β-FeCo-PCNF, showing the distribution of C, N, O, Co and Fe.

(Fig. S2). The transmission electron microscopy (TEM) images of FeCo-CNF show the presence of agglomerated metal particles with diameters of 70–140 nm (Fig. S3), which can induce large stress and break the nanofibers. In contrast, the TEM image of β-FeCo-PCNF displays an amorphous carbon structure with randomly oriented graphitic domains (Fig. 2b), and no obvious metal particles can be observed, further

supporting the role of β-CD as an isolator for metals. The high-angle annular dark field-scanning transmission electron microscopy (HAADF-STEM) image in Fig. 2c clearly shows the uniformly distributed metal species with an average size of ~1.0 nm, which can be distinguished by the high population of bright dots. The atomic-resolution HAADF-STEM image in Fig. 2d reveals the coexistence of metal atomic

clusters (as indicated by the yellow dashed circles) and single atom metal species. Moreover, the atomic distance between two adjacent metals is about 0.32 nm, confirming the presence of metal pairs (Fig. 2d, e), and the measured distance between Fe and Co is close to the theoretical calculation value of 0.317 nm based on the Fe-Co atomic pair sites (Fig. S5). The corresponding electron energy loss spectra (EELS) show the coexistence of Fe and Co in the atomic pair (Fig. 2f). Additionally, energy dispersive X-ray spectroscopy (EDXS) images show the distribution of Fe, Co, N, O, and C throughout the entire architecture (Fig. 2g), and the bright areas with the coexistence of Fe and Co further confirm the presence of Fe-Co alloy clusters.

Fig. 3a and Table S1 provide a detailed analysis of the textural properties of β-FeCo-PCNF and FeCo-CNF. The type I/IV isotherms of β-FeCo-PCNF and FeCo-CNF indicate the presence of both micropores and mesopores. The Brunauer-Emmett-Teller (BET) specific surface area and total pore volume of β-FeCo-PCNF ($1026 \ m^2 \ g^{-1}$/$0.98 \ cm^3 \ g^{-1}$) are significantly higher than those of FeCo-CNF ($681 \ m^2 \ g^{-1}$/$0.61 \ cm^3 \ g^{-1}$). The pore size distributions obtained by non-local density functional theory (NLDFT) for β-FeCo-PCNF and FeCo-CNF indicate that the introduction of β-CD results in a significant increase in the pore diameters ranging from 0.4 to 1.1 nm of β-FeCo-PCNF, leading to a rise in microporosity from 59% for FeCo-CNF to 75% for β-FeCo-PCNF. These results indicate that the inclusion of β-CD promotes the generation of a porous structure, which in turn exposes more active sites for catalytic reactions. The X-ray diffraction (XRD) patterns in Fig. 3b reveal that β-FeCo-PCNF not only exhibits a peak at 21.5° indexed to graphite, but also a peak at 44.5° indexed to FeCo alloy. In contrast, the XRD pattern of FeCo-CNF exhibits multiple characteristic peaks corresponding to $Co_{0.72}Fe_{0.28}$, CoFe, Fe_3O_4, CoO and $CoFe_2O_4$, in addition to the two broad diffraction peaks at 21.5° and 44.5°, demonstrating the presence of complex phases in FeCo-CNF due to the absence of protection from β-CD. Meanwhile, only the Fe/Co structure is observed in β-Fe-PCNF/β-Co-PCNF, which further proves that β-CD can effectively control the crystal structure of metals (Fig.S6).

Raman spectra shown in Fig. 3c exhibit characteristic disorder D-band ($1335 \ cm^{-1}$) and graphitic carbon-related G-band ($1580 \ cm^{-1}$) signals for both β-FeCo-PCNF and FeCo-CNF. The I_D/I_G ratio for β-FeCo-PCNF (1.61) is significantly higher than that of FeCo-CNF (1.29), indicating the presence of more defective sites induced by β-CD. The defects in catalysts play a crucial role in electrocatalytic oxygen reactions by altering the distribution of electron density and electronic charge of the catalysts[38,39]. Inductively coupled plasma optical emission spectrometry (ICP-OES) result demonstrates that the loading of Fe and Co atoms in β-FeCo-PCNF reaches 2.44 wt% and 1.29 wt%, respectively. The surface valence states of β-FeCo-PCNF were analyzed using X-ray photoelectron spectroscopy (XPS) (Fig. S6 and Table S2). The Fe/Co and N contents on the surface of β-FeCo-PCNF are estimated to be 1.01 at% and 3.02 at%. The high-resolution N 1 s spectra of β-FeCo-PCNF and FeCo-CNF are deconvoluted into five peaks at 397.6 eV (pyridinic-N), 398.5 eV (pyrrolic-N), 399.2 eV (metal-N), 400.2 eV (graphitic N), and 402.2 eV (oxidized N) (Fig. 3d and Table S3)[40]. The metal-N species in β-FeCo-PCNF (14.52%), which are considered as the main electrocatalytic active centers in ORR reaction[41], have higher content than those of FeCo-CNF (5.21%), β-Fe-PCNF (7.73%) and β-Co-PCNF (8.98%), suggesting that the introduction of β-CD and the metal pairs are more favorable for the formation of metal-N. The high-resolution spectrum of Co/Fe 2p for β-FeCo-PCNF and β-Fe-PCNF displayed four pairs of peaks, namely, the metallic state of Co^0/Fe^0, Co^{2+}/Fe^{2+}, Co^{3+}/Fe^{3+}, and satellite peaks (Fig. 3e and Fig. 3f)[42,43]. Compared to β-Co-PCNF and β-Fe-PCNF, the binding energies of metal Co^0 (-0.3 eV) and Fe^0 (-0.5 eV) in β-FeCo-PCNF are shifted to lower binding energies, indicating the presence of Fe-Co alloy clusters[44]. Notably, the main peaks of Co $2p_{3/2}$ (0.9 eV) and Fe $2p_{3/2}$ (0.6 eV) in β-FeCo-PCNF are respectively shifted to higher binding energies compared to β-Co-PCNF and β-Fe-PCNF, indicating a significant interaction between single-atomic metal sites and Fe-Co alloys clusters[45]. This interaction can alter the electronic structure of the single-atomic metal sites, optimizing the adsorption energy of the active sites for reactants and reaction intermediates. To determine the role of FeCo clusters, a sample of β-FeCo-PCNF-AC without FeCo clusters was prepared by acid corrosion of β-FeCo-PCNF. The absence of Co^0 and Fe^0 in β-FeCo-PCNF-AC indicates the washing out of Fe-Co alloy clusters (Fig. S11). Notably, both
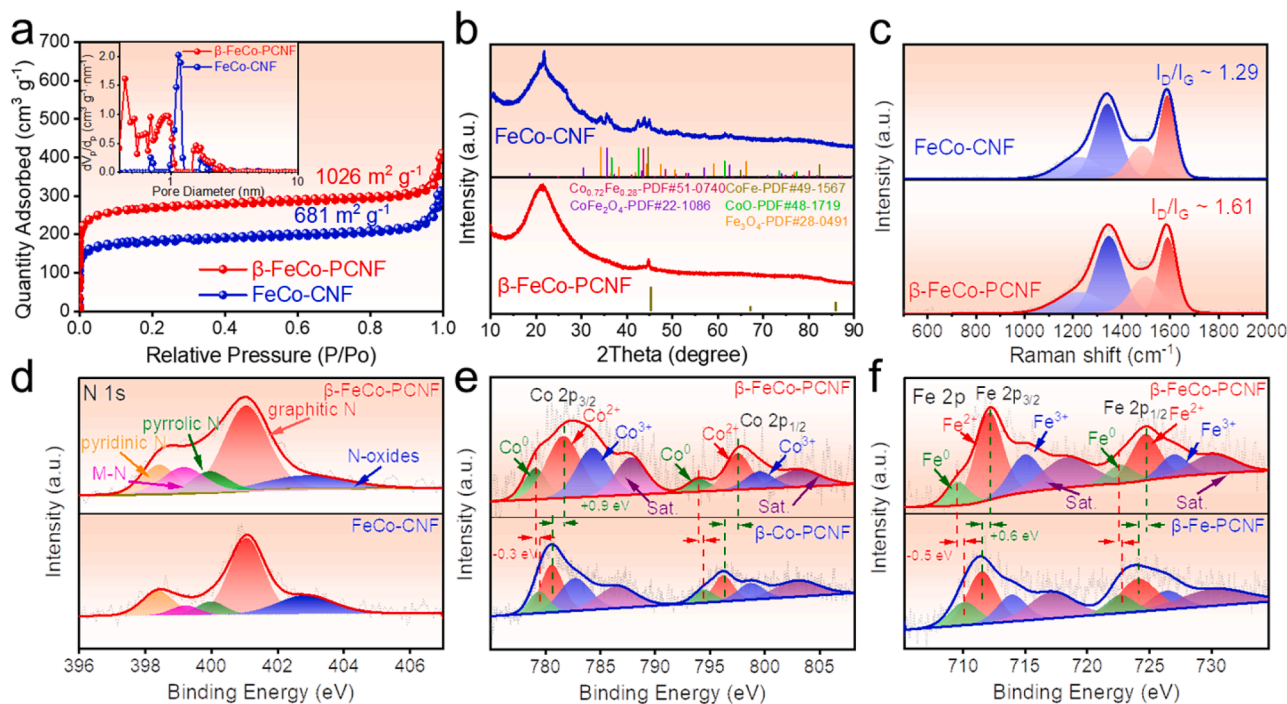

Fig. 3. (a) Nitrogen adsorption-desorption isotherms, with the inset showing the pore size distributions for β-FeCo-PCNF and FeCo-CNF. (b) XRD patterns of β-FeCo-PCNF and FeCo-CNF. (c) Raman spectra of β-FeCo-PCNF and FeCo-CNF. (d) XPS spectra of N 1 s for β-FeCo-PCNF and FeCo-PCNF. (e) XPS spectra of Co 2p for β-FeCo-PCNF and β-Co-PCNF. (f) XPS spectra of Fe 2p for β-FeCo-PCNF and β-Fe-PCNF.

Co 2p$_{3/2}$ and Fe 2p$_{3/2}$ in the β-FeCo-PCNF-AC are negatively shifted, giving initial evidence that the Fe-Co alloy clusters can adjust the Co/Fe single-atom electronic structure. Moreover, the almost identical nitrogen species in β-FeCo-PCNF and β-FeCo-PCNF-AC imply the stable structure of Co and Fe coordinated to N.

The synchrotron X-ray absorption spectroscopy technique was used to investigate the coordination environment of Fe and Co atoms in β-FeCo-PCNF. The Fe K-edge X-ray absorption near-edge structure (XANES) spectra in Fig. 4a indicate that the absorption edge of β-FeCo-PCNF is located between that of Fe foil and Fe$_2$O$_3$, suggesting an average oxidation state of 1.91 (Fig. S12). Fourier-transformed (FT) k^3-weighted extended X-ray absorption fine structure (EXAFS) spectra in Fig. 4b reveal the Fe-N scattering peak at 1.44 Å and the Fe-Co scattering peak at 2.11 Å, confirming the existence of single-atom Fe and Fe-Co alloy clusters in β-FeCo-PCNF. Additionally, a weak Fe-Co signal was detected at 2.76 Å, indicating that the presensce of Fe-Co bond with larger bond length and low coordination number in β-FeCo-PCNF. EXAFS fitting (Fig. 4c, Fig. S13 and Table S4) further reveals that the coordination number of the Fe-N path is approximately 3.8 with a bond length of 1.92 Å, indicating the formation of an Fe-N$_4$ moiety, and the calculated coordination numbers of the Fe-Co path are 1.8 with bond lengths of 2.48 Å, suggesting the formation of Fe-Co alloy clusters. Furthermore,

the longer bond length of Fe-Co in β-FeCo-PCNF was fitted with a coordination number of 0.8 and a bond lengths of 3.28 Å, indicating the presence of Fe-Co atomic pairs in β-FeCo-PCNF. Notably, the fitted bond length for Fe-Co atomic pairs is similar to the HADDF result and the theoretical calculation value. The same analysis process was carried out for the Co species. As shown in Fig. 4d and Fig. S14, the average oxidation state of Co in β-FeCo-PCNF is 1.33. Moreover, in the Co-EXAFS spectra of β-FeCo-PCNF (Fig. 4e), the fitting results depict two Co-N coordination numbers of 1.3 and 2.5, and the bond lengths are calculated to be 1.73 and 2.05 Å (Fig. 4f, Fig. S15 and Table S5), indicating the formation of asymmetric CoN$_4$ moiety. The reason for the formation of this asymmetric CoN$_4$ structure is related with the presence of FeCo alloy clusters. It is noteworthy that the fitting results for Fe-Co paths in the Co-EXAFS fitting are almost identical to those of the Fe-EXAFS fitting. Additionally, compared with the Fe/Co foil, the EXAFS wavelet transform plots of both Co and Fe for β-FeCo-PCNF exhibit two characteristic centers of Fe/Co-N and Fe-Co (Fig. 4g and Fig. 4h). Based on the above analysis, the atomic structure model of β-FeCo-PCNF consists of single-atom dispersed N$_4$Fe-CoN$_4$ atomic pairs and Fe-Co alloy clusters.
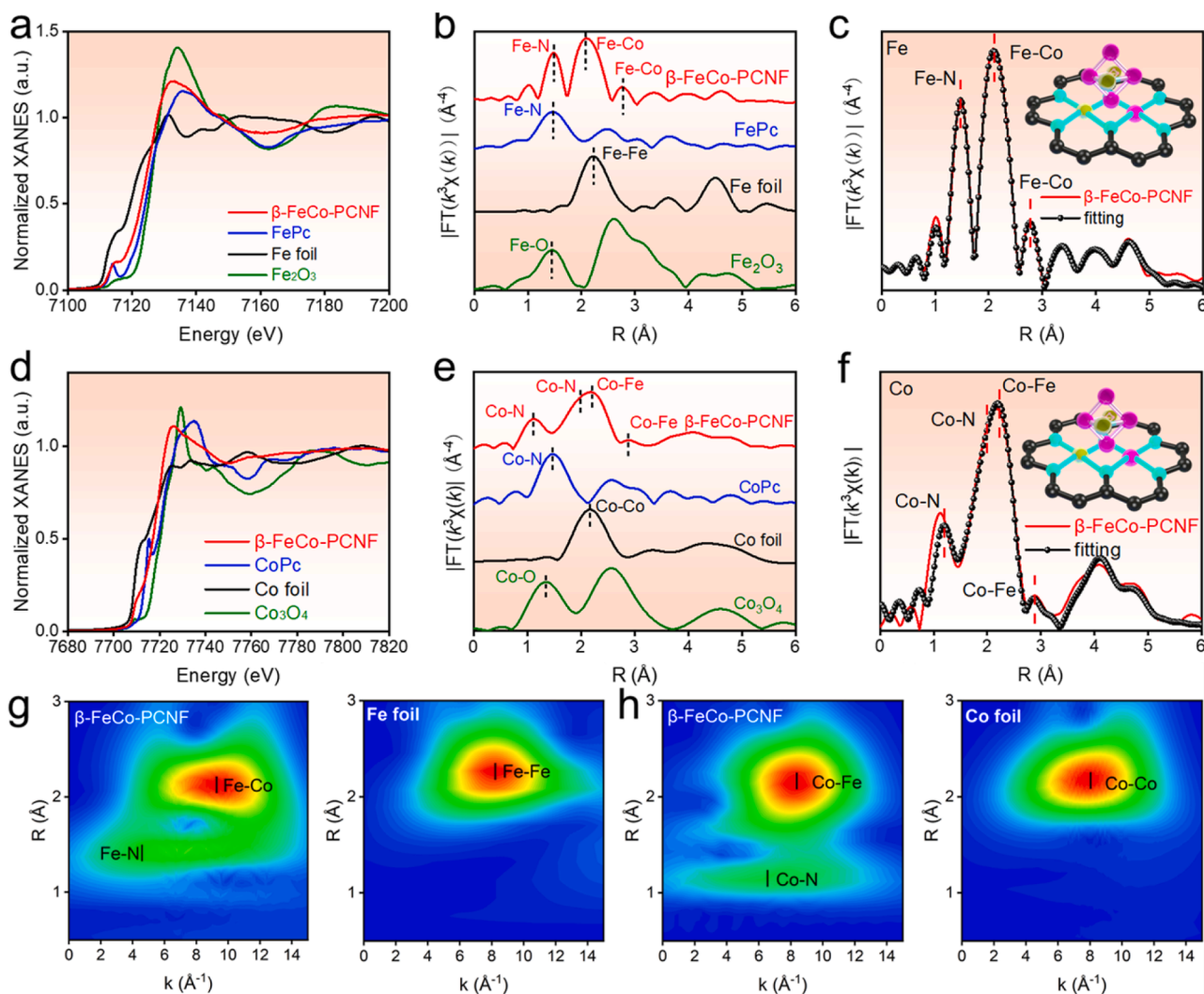

Fig. 4. (a) The Fe K-edge XANES spectra, and (b) k^3-weighted χ(k)-function of Fe-EXAFS spectra of β-FeCo-PCNF, FePc, Fe foil, FeO, and Fe$_2$O$_3$. (c) Fe-EXAFS fitting curves of β-FeCo-PCNF at R space. (d) The Co K-edge XANES spectra, and (e) k^3-weighted χ(k)-function of Co-EXAFS spectra of β-FeCo-PCNF, CoPc, Co foil, and Co$_3$O$_4$. (f) Co-EXAFS fitting curves of β-FeCo-PCNF at R space. (g) Fe k-edge WT-EXAFS spectra of β-FeCo-PCNF and Fe foil. (h) Co k-edge WT-EXAFS spectra of β-FeCo-PCNF and Co foil.

3.2. Electrocatalytic ORR and OER processes

The performance of electrochemical oxygen catalysis for the investigated catalysts was evaluated by rotating disk/ring-disk electrode (RDE/RRDE) measurements. As shown in 5a, for the ORR process, β-FeCo-PCNF has an onset potential (E_{onset}) of 1.01 V and half-wave potential ($E_{1/2}$) of 0.90 V, which is better than those of commercial Pt/C (E_{onset} = 0.98 V, $E_{1/2}$ = 0.83 V) and most of the reported catalysts (Table S6)[46–54]. The E_{onset} (0.95 V) and $E_{1/2}$ (0.83 V) values of β-FeCo-PCNF-AC are lower compared to those of β-FeCo-PCNF. However, they are comparable to the values of Pt/C and significantly superior to those of PCNF. These results suggest that the Fe-Co atomic pair sites exhibit exceptional catalytic activity towards the ORR reaction, and the presence of metallic Co-Fe clusters further enhances the ORR performance of the Fe-Co atomic pair sites. As shown in Fig.S16, compared to β-FeCo-PCNF, the β-Fe-PCNF and β-Co-PCNF electrocatalysts display smaller catalytic activity due to the absence of the synergy between Fe and Co. Besides, FeCo-CNF without enough atomic metal sites and the small metal clusters exhibits the worst ORR activities (E_{onset} = 0.89 V, $E_{1/2}$ = 0.78 V). As shown in Fig. 5b, the Tafel slope of β-FeCo-PCNF is approximately 58 mV dec^{-1} for the ORR, which is lower than those obtained for FeCo-CNF (68 mV dec^{-1}), β-FeCo-PCNF-AC (62 mV dec^{-1})

PCNF (102 mV dec^{-1}) and commercial Pt/C (73 mV dec^{-1}), demonstrating faster reaction kinetics for β-FeCo-PCNF. The electron transfer number (n) and yield of peroxide percentage (H$_2$O$_2$%) was calculated using the RRDE technique (Fig. S17). The results show that the H$_2$O$_2$% yield of β-FeCo-PCNF remains below 5.7% over the potential range of 0.3–0.8 V. The average electron transfer number (n) of β-FeCo-PCNF abstained from the RRDE test is above 3.91. Fig. S18a shows LSV curves of β-FeCo-PCNF under different rotation speeds, and the corresponding K-L plots reveal an average n of 4 within the potentials range of 0.3–0.7 V (Fig. S18b), which is consistent with the results obtained from the RRDE test, indicating that the β-FeCo-PCNF has very high ORR catalytic selectivity. As depicted in Fig. S19, the current curve of β-FeCo-PCNF remains stable subsequent to methanol injection into the electrolyte, whereas the commercial Pt/C catalyst experiences a sharp decay of current density owing to the well-known methanol poisoning effect on Pt catalysts. In the chronoamperometric (i-t) test (Fig. 5c), the initial current density of β-FeCo-PCNF is relative lower than that of Pt/C, however, the current retention of β-FeCo-PCNF after testing is 90.0%, surpassing that of Pt/C (84.3%). This remarkable result demonstrates the excellent stability of β-FeCo-PCNF.

The OER polarization curves are compared in Fig. 5d. The β-FeCo-PCNF possesses the OER potential of 1.495 V at 10 mA cm^{-2} ($E_{j=10}$),
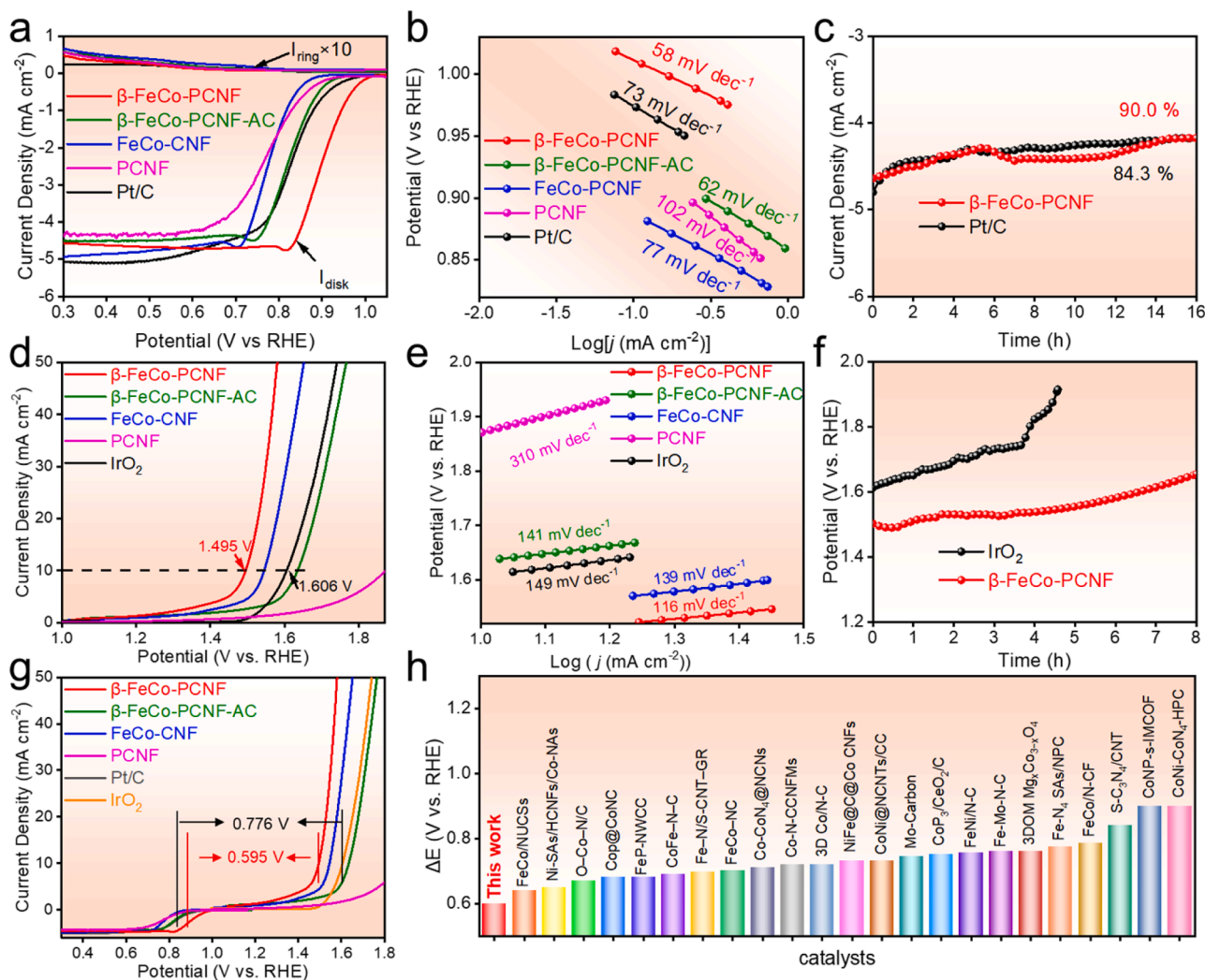

Fig. 5. (a) ORR LSV curves, and (b) the ORR Tafel plots for the β-FeCo-PCNF, β-FeCo-PCNF-AC, FeCo-CNF, PCNF and Pt/C. (c) Stability tests of the β-FeCo-PCNF and Pt/C for ORR at 0.6 V. (d) OER LSV curves measured in 1 M KOH, and (e) the corresponding OER Tafel plots of the β-FeCo-PCNF, β-FeCo-PCNF-AC, FeCo-CNF, PCNF and IrO$_2$. (f) Stability tests of the β-FeCo-PCNF and IrO$_2$ for OER at 10 mA cm^{-2}. (g) The overall LSV curves of β-FeCo-PCNF, β-FeCo-PCNF-AC, FeCo-CNF, PCNF, Pt/C and IrO$_2$ for ORR and OER. (h) Comparisons of the ΔE of β-FeCo-PCNF with other reported catalysts.

apparently lower than those of FeCo-CNF (1.545 V), β-FeCo-PCNF-AC (1.634 V), PCNF (1.864 V) and IrO$_2$ (1.606 V). After the removal of the metallic FeCo phase, the OER performance of β-FeCo-PCNF-AC exhibits a steep decline, dropping below that of IrO$_2$. This emphasizes the notable contribution of FeCo clusters within the β-FeCo-PCNF structure in enhancing the OER capability. Moreover, the OER catalytic activity of β-FeCo-PCNF-AC outperforms that of PCNF, highlighting the exceptional OER performance of the Fe-Co atomic pair sites. The absence of synergistic interaction between Fe and Co results in the much lower OER catalytic activity for both β-Fe-PCNF ($E_{j=10}$ = 1.662 V) and β-Co-PCNF ($E_{j=10}$ = 1.644 V) than that of β-FeCo-PCNF (Fig. S20). Correspondingly, β-FeCo-PCNF also exhibits a smaller Tafel slope of 116 mV dec^{-1}, illustrating its fast kinetics in the OER process (Fig. 5e). Moreover, the β-FeCo-PCNF catalyst demonstrates well durability during chronopotentiometry response measurements, which is better than the commercial IrO$_2$ (Fig. 5f). The electrochemical surface area (ECSA) was assessed by electrochemical double-layer capacitance (C_{dl}) in the non-Faraday region. As shown in Fig. S21, β-FeCo-PCNF exhibits a higher C_{dl} (72.9 mF cm^{-2}) than those of FeCo-CNF (56.5 mF cm^{-2}), β-FeCo-PCNF-AC (19.9 mF cm^{-2}), β-Co-PCNF (30.9 mF cm^{-2}), and β-Fe-PCNF (66.9 mF cm^{-2}), demonstrating more exposed active sites in β-FeCo-PCNF. This suggests that the introduction of β-CD and smaller alloy clusters are crucial for increasing active site exposure, allowing more active sites to participate in the reaction. The overall bifunctional oxygen electrocatalysis property was further evaluated through the potential gap (ΔE) between the $E_{1/2}$ of ORR and the $E_{j=10}$ of OER. As shown in

Fig. 5g-h, the β-FeCo-PCNF has a lower ΔE value of about 0.595 V than that of FeCo-CNF (0.765 V), β-FeCo-PCNF-AC (0.804 V), PCNF (1.094 V) and most reported bifunctional catalysts,[36,44,55–75] which proves β-FeCo-PCNF has excellent reversible oxygen electrode performance. The effects of pyrolysis temperature, the used amount of metal salts, and the mole ratio of Fe(NO$_3$)$_3$·9 H$_2$O and Co(NO$_3$)$_2$·6 H$_2$O for the synthesized β-FeCo-PCNF on the ORR and OER catalytic activities were also investigated. By comparing the catalytic performance of samples prepared at different pyrolysis temperatures, the optimal temperature for catalyst formation was determined to be 1000 °C (Fig. S22). As shown in Fig. S23, using a total amount of 0.15 mmol for Fe (NO$_3$)$_3$·9 H$_2$O and Co(NO$_3$)$_2$·6 H$_2$O with a molar ratio of 2:1, the prepared β-FeCo-PCNF presented the best performance in terms of the catalytic properties of ORR and OER.

3.3. Mechanism Exploration

Density functional theory (DFT) calculations were conducted to investigate the specific role of Fe-Co alloy clusters in influencing the catalytic properties of FeN$_4$-CoN$_4$ atom pairs. The theoretical model consisted of FeN$_4$-CoN$_4$ atom pairs and Fe-Co alloy clusters (denoted as FeCo$_{ac}$/FeN$_4$-CoN$_4$) are shown in Fig. 6a. In order to investigate the effect of Fe-Co alloy clusters on the electronic structure of FeN$_4$-CoN$_4$ atom pairs, the charge density differences were analyzed. The charge density differences infer that Fe-Co alloy clusters make the Fe site of FeN$_4$-CoN$_4$ atom pairs become less positive, which is beneficial for
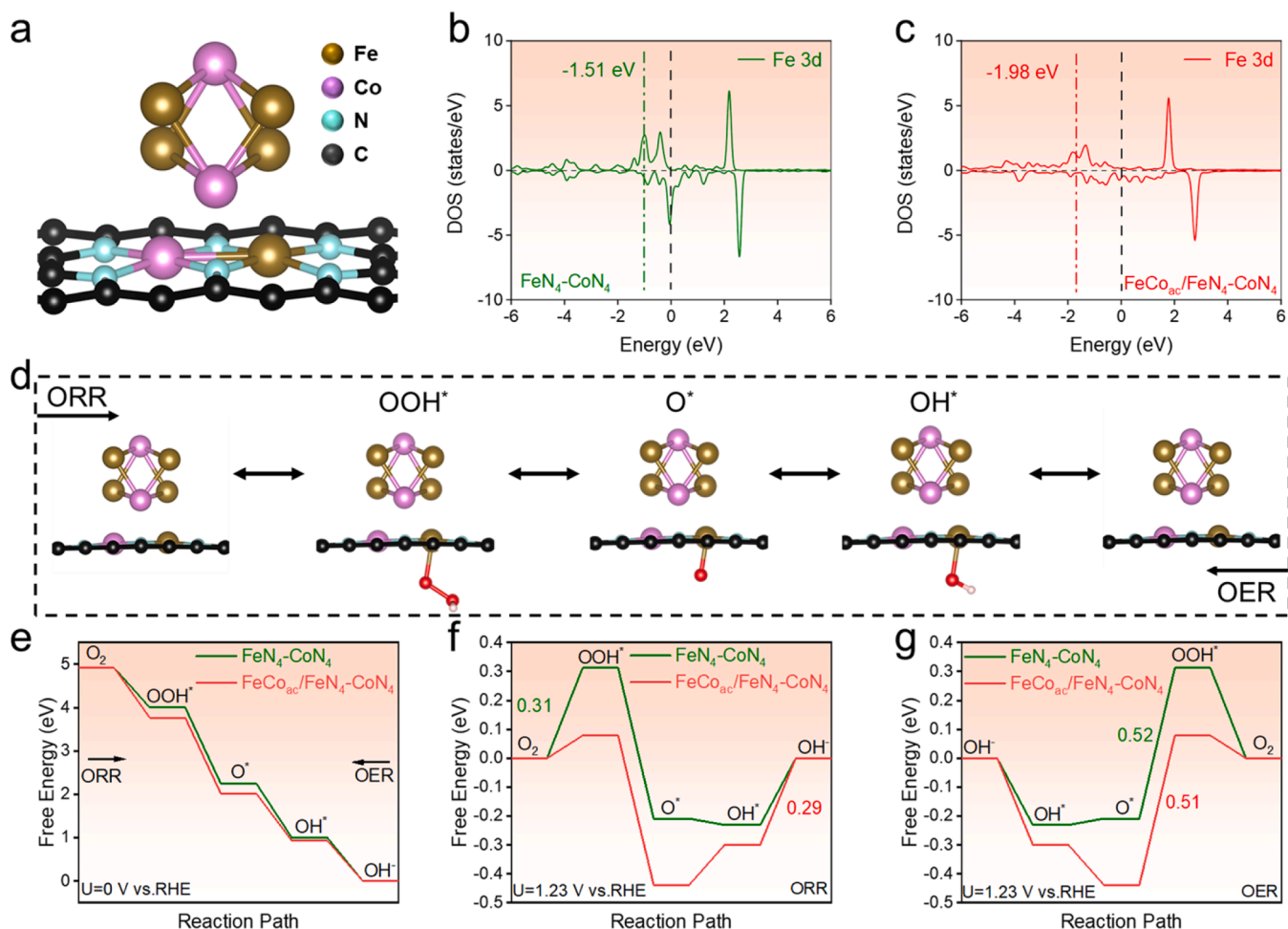

Fig. 6. (a) The optimized structure models of FeCo$_{ac}$/FeN$_4$-CoN$_4$. (b) PDOS of modelling structure of FeN$_4$-CoN$_4$. (c) PDOS of modelling structure of FeCo$_{ac}$/FeN$_4$-CoN$_4$. (d) Proposed ORR and OER mechanisms of FeCo$_{ac}$/FeN$_4$-CoN$_4$ structure. Free energy diagrams of different intermediates on FeCo$_{ac}$/FeN$_4$-CoN$_4$ and FeN$_4$-CoN$_4$ (e) at U = 0 V, (f) at U = 1.23 V for ORR and (g) at U = 1.23 V for OER.

optimizing the adsorption/desorption performance of the ORR/OER reaction intermediates, thereby achieving an enhancement in reaction activity and kinetics (Fig. S24). As indicated by the projected density of states (PDOS) in Fig. 6b and Fig. 6c, the corresponding *d*-band center relative to Fermi level of Fe in $FeCo_{ac}/FeN_4-CoN_4$ (−1.98 eV) exhibits a downshift compared to FeN_4-CoN_4 (−1.51 eV), indicating that the introduction of Fe-Co alloy clusters results in a reduction in the strength of the interaction of the reactants with the Fe active site, thereby optimizing the free energy of the reaction. To validate the results, Gibbs free energy calculations were carried out on the single atom Fe active sites of $FeCo_{ac}/FeN_4-CoN_4$ and FeN_4-CoN_4 models. The optimized structures of the OH*, O*, and OOH* intermediates on $FeCo_{ac}/FeN_4-CoN_4$ and FeN_4-CoN_4 are shown in Fig. 6d and Fig. S25. The free energy diagrams in Fig. 6e demonstrate that all the reaction steps on $FeCo_{ac}/FeN_4-CoN_4$ and FeN_4-CoN_4 are downhill at U= 0 V, indicating that the ORR process is exothermic and can be carried out spontaneously on the catalyst surface. However, when the potential is increased to the equilibrium potential (U=1.23 V), several endothermic ORR pathways are appeared (Fig. 6f). The rate-determining step (RDS) on FeN_4-CoN_4 is the hydrogenation of molecular O_2 with a limiting barrier of 0.31 eV. In contrast, the RDS for

the Fe site assisted by Fe-Co alloy clusters in $FeCo_{ac}/FeN_4-CoN_4$ is the protonation of OH* with a decreased limiting barrier of 0.29 eV. This highlights the critical role of Fe-Co alloy clusters in energetically facilitating the ORR process. With respect to OER (Fig. 6g), the RDS of $FeCo_{ac}/FeN_4-CoN_4$ and FeN_4-CoN_4 is the formation of OOH*. The smaller OER overpotential of $FeCo_{ac}/FeN_4-CoN_4$ (0.51 V) than that of FeN_4-CoN_4 (0.52 V) also reveals the promoted OER activity of Fe active sites by Fe-Co alloy clusters. Overall, DFT calculations provide evidence that the electronic structure of Fe-Co atomic pairs is optimized by Fe-Co alloy clusters, resulting in superior bifunctional properties of β-FeCo-PCNF.

To investigate the stable chemical composition features of β-FeCo-PCNF, we analyzed its XANES and EXAFS spectra after ORR and OER. Fig. S26a shows that the absorption edge of β-FeCo-PCNF-post ORR is similar to that of β-FeCo-PCNF. Additionally, the fitting results of the Fe K-edge EXAFS show that β-FeCo-PCNF-post ORR has similar peaks to those of β-FeCo-PCNF, with a local structure composed of Fe single atoms with Fe-N4 structure, Fe-Co clusters, and Fe-Co atomic pairs (Fig. S26b, Fig. S26c, and Table S7). Therefore, the β-FeCo-PCNF still retains its initial chemical state after ORR stability testing. On the other
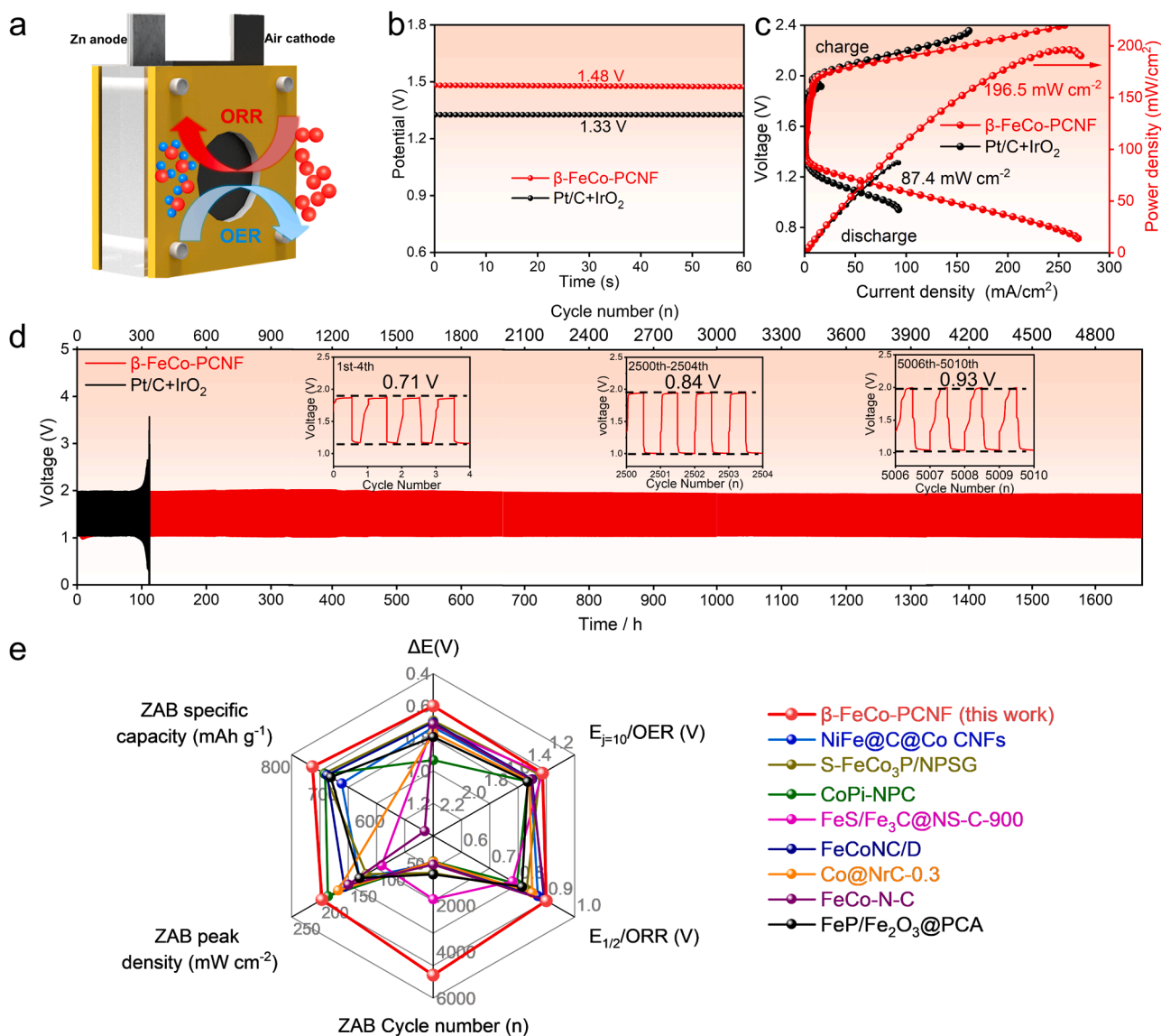

Fig. 7. (a) Schematic diagram of rechargeable Zn-air battery. (b) The open circuit voltage of β-FeCo-PCNF and Pt/C+IrO₂ based Zn-air batteries. (c) Polarization and power density curves of β-FeCo-PCNF and Pt/C+IrO₂ based Zn-air batteries. (d) Galvanostatic charge-discharge test of β-FeCo-PCNF and Pt/C+IrO₂ based Zn-air batteries at 10 mA cm⁻². (e) Comprehensive comparison of the performance of β-FeCo-PCNF with other reported catalysts.

hand, Fig. S27a shows that the absorption edge of β-FeCo-PCNF-post OER is more positive than that of β-FeCo-PCNF, suggesting an increase in the oxidation state of the Fe atoms after OER. The Fe K-edge EXAFS shows that the first peak of β-FeCo-PCNF-post OER is shifted to the right compared to that of β-FeCo-PCNF (Fig. S27b). According to the fitting results (Fig. S27c and Table S8), the local structure of β-FeCo-PCNF-post OER is composed of Fe single atoms with Fe-N$_4$O$_2$, Fe-Co clusters, and Fe-Co atomic pairs. These results indicate that the single active metal Fe sites attain high-valence states due to the formation of HOO-Fe-N$_4$ moieties during catalytic activation. Therefore, we propose that the formation of high-valence HOO-Fe-N$_4$ moieties under working conditions is responsible for the reactivity toward OER[76].

3.4. Electrochemical evaluation of Zn-air battery

Based on the excellent bifunctionality of β-FeCo-PCNF, a homemade Zn-air battery was assembled by using β-FeCo-PCNF as air cathode, Zn plate as anode, and a 6 M KOH and 0.2 M Zn (Ac)$_2$ mixed solution as the electrolyte (Fig. 7a). Another Zn-air battery assembled by using Pt/C+IrO$_2$ (1:1 wt ratio) as air cathode was also built for comparison. As shown in Fig. 7b, the Zn-air battery assembled with β-FeCo-PCNF exhibits an open-circuit voltage of 1.48 V, which is much higher than that of Pt/C+IrO$_2$ (1.33 V). The charge-discharge curves of β-FeCo-PCNF based Zn-air battery shows a smaller charge/discharge voltage gap (0.71 V @ 10 mA cm^{-2}) than that of Pt/C+IrO$_2$ (0.76 V @ 10 mA cm^{-2}), implying excellent reversible oxygen catalytic activity (Fig. 7c). The peak power density of β-FeCo-PCNF based Zn-air battery is 196.5 mW cm^{-2}, greater than that of Pt/C+IrO$_2$ (87.4 mW cm^{-2}) and other reported catalysts (Table S9) [77–83]. As shown in Fig. S28, the gravimetric energy density of β-FeCo-PCNF based Zn-air battery normalized to the mass of consumed Zn is estimated to be 756 mAh g^{-1}, superior to the Pt/C+IrO$_2$ based Zn-air battery (713 mAh g^{-1}). Besides, the long-term galvanostatic cycling tests (Fig. 7d) show that the β-FeCo-PCNF based Zn-air battery exhibits outstanding charge-discharge cycle durability for over 1670 h (5010 cycles) at current density of 10 mA cm^{-2}, far more outperforming the Pt/C+IrO$_2$ based Zn-air battery. Specifically, the charge/discharge voltage gap of the β-FeCo-PCNF based Zn-air battery in first cycle is only 0.78 V, and round-trip efficiency is 61%. Surprisingly, β-FeCo-PCNF based Zn-air battery still maintains a small voltage gap of 0.93 V with a high energy efficiency of 52% over continuous 5010 cycles.

Compared with recently reported catalysts (Fig. 7e)[64,84–90], the β-FeCo-PCNF catalyst displays superior performance in terms of the ORR ($E_{1/2}$), OER ($E_{j=10}$), potential gap (ΔE) between the $E_{1/2}$ of ORR and the $E_{j=10}$ of OER, peak power density of Zn-air battery, specific capacity, and cycle durability of Zn-air battery. The excellent bifunctional activity of β-FeCo-PCNF can be attributed to several features: Firstly, the proposed isolation-confinement strategy with the assistance of β-CD confines the metal ions for forming the single-atomic metal sites and limits the size of Fe-Co alloys to nanoscale, thus enabling the high utilization of Fe-Co alloy. Secondly, the electronic structure of Fe-Co atom pairs is modulated by Fe-Co alloys clusters, optimizing the adsorption/desorption energy of the ORR/OER reaction intermediates and improving the intrinsic catalytic activity of Fe-Co atom pairs. Thirdly, The Fe-Co alloy clusters not only enhance the intrinsic activity of Fe-Co atomic pairs, but they also exhibit significant OER activity, thereby increasing the active site density of the catalyst. Last but not the least, the large specific surface area with interconnected porous structure induced by the decomposition of β-CD allows an abundance of active sites to be exposed on the surface, facilitating the rapid mass/electron transfer.

4. Conclusion

In summary, we have developed a novel and straightforward isolation-confinement strategy to efficiently synthesize Fe-Co atom pairs and Fe-Co clusters anchored on N, porous carbon fibers catalyst with the assistance of β-CD. The combination of experimental data and theoretical results leads to the essential conclusion that the presence of Fe-Co alloy clusters effectively changes the electronic structure of the Fe-Co atom pairs, resulting in a down-shift of the ᴅ-band center. This structural modification is found to be conducive to obtaining the best adsorption/desorption performance of the ORR/OER reaction intermediates. The designed β-FeCo-PCNF catalyst exhibits excellent ORR $E_{1/2}$ of 0.90 V and OER $E_{j=10}$ of 1.495 V. Additionally, the β-FeCo-PCNF-based Zn-air battery exhibited a large power density of 196.5 mW·cm^{-2} and excellent stability, with no noticeable voltage changes observed even after 1670 h. The reported concept in designing bifunctional catalyst could be widely adapted to fabricate potential metal alloy cluster (such as FeNi, FeMn, CoMn, FeCu)-decorated single-atomic metal sites catalysts, and this study also opens up new opportunities for enhancing the intrinsic activity of single-atom catalysts for various electrochemical reactions beyond ORR/OER.

CRediT authorship contribution statement

Ping Li: Conceptualization, Methodology, Investigation, Formal analysis, Data curation, Writing – original draft. **Qiang Fuqiang:** Investigation, Formal analysis, Data curation. **Xuehai Tan**: Investigation, Formal analysis. **Zhi Li**: Supervision, Writing – review & editing, Project administration, Funding acquisition. **Jing Shi**: Investigation, Validation. **Shuai Liu**: Investigation, Visualization. **Minghua Huang:** Investigation, Data curation. **Jingwei Chen**: Resources, Supervision. **Weiqian Tian**: Investigation, Formal analysis. **Jingyi Wu**: Supervision, Resources. **Wei Hu**: Methodology, Data curation. **Huanlei Wang**: Supervision, Writing – review & editing, Project administration, Funding acquisition.

Declaration of Competing Interest

The authors declare that they have no known competing financial interests or personal relationships that could have appeared to influence the work reported in this paper.

Data availability

Data will be made available on request.

Acknowledgements

Appendix A. Supporting information

Supplementary data associated with this article can be found in the online version at doi:10.1016/j.apcatb.2023.123231.

References

[1] Y. Cheng, X. Gong, S. Tao, L. Hu, W. Zhu, M. Wang, J. Shi, F. Liao, H. Geng, M. Shao, Mechano-thermal milling synthesis of atomically dispersed platinum with spin polarization induced by cobalt atoms towards enhanced oxygen reduction reaction, Nano Energy 98 (2022), 107341, https://doi.org/10.1016/j.nanoen.2022.107341.

[2] J. Dai, J. Zhang, R. Karthick, M. Liang, Q. Wei, X. Chen, Y. Shi, S. Zhai, G. Wang, F. Chen, Co/Fe$_3$O$_4$ nanoparticles embedded in N-doped hierarchical porous carbon derived from zeolitic imidazolate frameworks as efficient oxygen reduction electrocatalysts for zinc–air battery-based desalination, J. Mater. Chem. A 10 (2022) 12213–12224, https://doi.org/10.1039/D2TA00736C.

[3] F. Lu, K. Fan, L. Cui, B. Li, Y. Yang, L. Zong, L. Wang, Engineering FeN$_4$ active sites onto nitrogen-rich carbon with tubular channels for enhanced oxygen reduction

reaction performance, Appl. Catal. B Environ. 313 (2022), 121464, https://doi.org/10.1016/j.apcatb.2022.121464.

[4] J. Chang, G. Wang, Y. Yang, Recent advances in electrode design for rechargeable zinc–air batteries, Small Sci. 1 (2021), 2100044, https://doi.org/10.1002/smsc.202100044.

[5] C. Fan, X. Wang, X. Wu, Y. Chen, Z. Wang, M. Li, D. Sun, Y. Tang, G. Fu, Neodymium-evoked valence electronic modulation to balance reversible oxygen electrocatalysis, Adv. Energy Mater. 13 (2023), 2203244, https://doi.org/10.1002/aenm.202203244.

[6] Y. Hu, X. Guo, T. Shen, Y. Zhu, D. Wang, Hollow porous carbon-confined atomically ordered $PtCo_3$ intermetallics for an efficient oxygen reduction reaction, ACS Catal. 12 (2022) 5380–5387, https://doi.org/10.1021/acscatal.2c01541.

[7] C. Yao, J. Li, Z. Zhang, C. Gou, Z. Zhang, G. Pan, J. Zhang, Hierarchical core–shell Co_2N/CoP embedded in N, P-doped carbon nanotubes as efficient oxygen reduction reaction catalysts for Zn-air batteries, Small 18 (2022), 2108094, https://doi.org/10.1002/smll.202108094.

[8] C. Xia, Y. Zhou, C. He, A.I. Douka, W. Guo, K. Qi, B.Y. Xia, Recent advances on electrospun nanomaterials for zinc–air batteries, Small Sci. 1 (2021), 2100010, https://doi.org/10.1002/smsc.202100010.

[9] R. Zhao, Z. Chen, Q. Li, X. Wang, Y. Tang, G. Fu, H. Li, J.-M. Lee, S. Huang, N-doped $LaPO_4$: an effective Pt-free catalyst for electrocatalytic oxygen reduction, Chem. Catal. 2 (2022) 3590–3606, https://doi.org/10.1016/j.checat.2022.11.008.

[10] X. Zhong, Y. Shao, B. Chen, C. Li, J. Sheng, X. Xiao, B. Xu, J. Li, H.-M. Cheng, G. Zhou, Rechargeable Zinc–Air batteries with an ultralarge discharge capacity per cycle and an ultralong cycle life, Adv. Mater. 35 (2023), 2301952, https://doi.org/10.1002/adma.202301952.

[11] P. Yin, T. Yao, Y. Wu, L. Zheng, Y. Lin, W. Liu, H. Ju, J. Zhu, X. Hong, Z. Deng, G. Zhou, S. Wei, Y. Li, Single cobalt atoms with precise N-coordination as superior oxygen reduction reaction catalysts, Angew. Chem. Int. Ed. 55 (2016) 10800–10805, https://doi.org/10.1002/anie.201604802.

[12] G. Xiao, R. Lu, J. Liu, X. Liao, Z. Wang, Y. Zhao, Coordination environments tune the activity of oxygen catalysis on single atom catalysts: a computational study, Nano Res. 15 (2022) 3073–3081, https://doi.org/10.1007/s12274-021-3964-0.

[13] P. Rao, D. Wu, T.-J. Wang, J. Li, P. Deng, Q. Chen, Y. Shen, Y. Chen, X. Tian, Single atomic cobalt electrocatalyst for efficient oxygen reduction reaction, eScience 2 (2022) 399–404, https://doi.org/10.1016/j.esci.2022.05.004.

[14] Q. Wang, Q. Feng, Y. Lei, S. Tang, L. Xu, Y. Xiong, G. Fang, Y. Wang, P. Yang, J. Liu, W. Liu, X. Xiong, Quasi-solid-state Zn-air batteries with an atomically dispersed cobalt electrocatalyst and organohydrogel electrolyte, Nat. Commun. 13 (2022) 3689, https://doi.org/10.1038/s41467-022-31383-4.

[15] Z. Li, B. Li, C. Yu, Atomic aerogel materials (or single atom aerogels): an interesting new paradigm in materials science and catalysis science, Adv. Mater. 35 (2023), 2211221, https://doi.org/10.1002/adma.202211221.

[16] H. Tian, A. Song, P. Zhang, K. Sun, J. Wang, B. Sun, Q. Fan, G. Shao, C. Chen, H. Liu, Y. Li, G. Wang, High durability of Fe–N–C single-atom catalysts with carbon vacancies toward the oxygen reduction reaction in alkaline media, Adv. Mater., 35 2210714. https://doi.org/10.1002/adma.202210714.

[17] Z. Li, B. Li, Y. Hu, S. Wang, C. Yu, Highly-dispersed and high-metal-density electrocatalysts on carbon supports for the oxygen reduction reaction: from nanoparticles to atomic-level architectures, Mater. Adv. 3 (2022) 779–809, https://doi.org/10.1039/D1MA00858G.

[18] G. Yasin, S. Ali, S. Ibraheem, A. Kumar, M. Tabish, M.A. Mushtaq, S. Ajmal, M. Arif, M.A. Khan, A. Saad, L. Qiao, W. Zhao, Simultaneously engineering the synergistic-effects and coordination-environment of dual-single-atomic iron/cobalt-sites as a bifunctional oxygen electrocatalyst for rechargeable zinc-air batteries, ACS Catal. 13 (2023) 2313–2325, https://doi.org/10.1021/acscatal.2c05654.

[19] H. Liu, L. Jiang, Y. Wang, X. Wang, J. Khan, Y. Zhu, J. Xiao, L. Li, L. Han, Boosting oxygen reduction with coexistence of single-atomic Fe and Cu sites decorated nitrogen-doped porous carbon, Chem. Eng. J. 452 (2023) 138938, https://doi.org/10.1016/j.cej.2022.138938.

[20] Y. Wu, C. Ye, L. Yu, Y. Liu, J. Huang, J. Bi, L. Xue, J. Sun, J. Yang, W. Zhang, X. Wang, P. Xiong, J. Zhu, Soft template-directed interlayer confinement synthesis of a Fe-Co dual single-atom catalyst for Zn-air batteries, Energy Stor. Mater. 45 (2022) 805–813, https://doi.org/10.1016/j.ensm.2021.12.029.

[21] T. Gu, D. Zhang, Y. Yang, C. Peng, D. Xue, C. Zhi, M. Zhu, J. Liu, Dual-Sites coordination engineering of single atom catalysts for full-temperature adaptive flexible ultralong-life solid-state Zn–air batteries, Adv. Funct. Mater. 33 (2023), 2212299, https://doi.org/10.1002/adfm.202212299.

[22] S. Sarkar, A. Biswas, E.E. Siddharthan, R. Thapa, R.S. Dey, Strategic modulation of target-specific isolated Fe,Co single-atom active sites for oxygen electrocatalysis impacting high power Zn–air battery, ACS Nano 16 (2022) 7890–7903, https://doi.org/10.1021/acsnano.2c00547.

[23] Z. Zhu, H. Yin, Y. Wang, C.-H. Chuang, L. Xing, M. Dong, Y.-R. Lu, G. Casillas-Garcia, Y. Zheng, S. Chen, Y. Dou, P. Liu, Q. Cheng, H. Zhao, Coexisting single-atomic Fe and Ni sites on hierarchically ordered porous carbon as a highly efficient ORR electrocatalyst, Adv. Mater. 32 (2020), 2004670, https://doi.org/10.1002/adma.202004670.

[24] X. Zhong, S. Ye, J. Tang, Y. Zhu, D. Wu, M. Gu, H. Pan, B. Xu, Engineering Pt and Fe dual-metal single atoms anchored on nitrogen-doped carbon with high activity and durability towards oxygen reduction reaction for zinc-air battery, Appl. Catal. B Environ. 286 (2021), 119891, https://doi.org/10.1016/j.apcatb.2021.119891.

[25] X. Cheng, Y. Wang, Y. Lu, L. Zheng, S. Sun, H. Li, G. Chen, J. Zhang, Single-atom alloy with Pt-Co dual sites as an efficient electrocatalyst for oxygen reduction reaction, Appl. Catal. B Environ. 306 (2022) 121112, https://doi.org/10.1016/j.apcatb.2022.121112.

[26] X. Zhu, T. Jin, C. Tian, C. Lu, X. Liu, M. Zeng, X. Zhuang, S. Yang, L. He, H. Liu, S. Dai, In situ coupling strategy for the preparation of FeCo alloys and Co_4N hybrid for highly efficient oxygen evolution, Adv. Mater. 29 (2017), 1704091, https://doi.org/10.1002/adma.201704091.

[27] J. Sun, N. Guo, T. Song, Y.-R. Hao, J. Sun, H. Xue, Q. Wang, Revealing the interfacial electron modulation effect of CoFe alloys with CoC_X encapsulated in N-doped CNTs for superior oxygen reduction, Adv. Powder Mater 1 (2022), 100023, https://doi.org/10.1016/j.apmate.2021.11.009.

[28] H. Huang, D. Yu, F. Hu, S.-C. Huang, J. Song, H.-Y. Chen, L.L. Li, S. Peng, Clusters induced electron redistribution to tune oxygen reduction activity of transition metal single-atom for metal–air batteries, Angew. Chem. Int. Ed. 61 (2022), e202116068, https://doi.org/10.1002/anie.202116068.

[29] M. Xu, C. Lai, X. Liu, B. Li, M. Zhang, F. Xu, S. Liu, L. Li, L. Qin, H. Yi, Y. Fu, COF-confined catalysts: from nanoparticles and nanoclusters to single atoms, J. Mater. Chem. A 9 (2021) 24148–24174, https://doi.org/10.1039/D1TA04439G.

[30] Covalent organic frameworks promoted single metal atom catalysis: Strategies and applications, in: V. Hasija, S. Patial, P. Raizada, A. Aslam Parwaz Khan, A.M. Asiri, Q. Van Le, V.-H. Nguyen, P. Singh (Eds.), Coord. Chem. Rev., 452, 2022, https://doi.org/10.1016/j.ccr.2021.214298.

[31] X. Guan, F. Chen, S. Qiu, Q. Fang, Three-dimensional covalent organic frameworks: from synthesis to applications, Angew. Chem. Int. Ed. 62 (2023), e202213203, https://doi.org/10.1002/anie.202213203.

[32] S. Zheng, S. Xia, S. Han, F. Yao, H. Zhao, M. Huang, β-Cyclodextrin-loaded minerals as novel sorbents for enhanced adsorption of Cd^{2+} and Pb^{2+} from aqueous solutions, Sci. Total Environ. 693 (2019), 133676, https://doi.org/10.1016/j.scitotenv.2019.133676.

[33] F. Wang, C. Li, J. Zhong, Z. Yang, A flexible core-shell carbon layer MnO nanofiber thin film via host-guest interaction: construction, characterization, and electrochemical performances, Carbon 128 (2018) 277–286, https://doi.org/10.1016/j.carbon.2017.11.075.

[34] W. Shi, B. Hu, H. Zhang, J. Li, J. Yang, J. Liu, Carbon-encapsulated iron oxide nanoparticles in self-supporting carbon nanofiber for high-performance supercapacitor in acid electrolyte with superior stability, ACS Appl. Energy Mater. 3 (2020) 12652–12661, https://doi.org/10.1021/acsaem.0c02571.

[35] G. Zhu, H. Yang, Y. Jiang, Z. Sun, X. Li, J. Yang, H. Wang, R. Zou, W. Jiang, P. Qiu, W. Luo, Modulating the electronic structure of FeCo nanoparticles in N-Doped mesoporous carbon for efficient oxygen reduction reaction, Adv. Sci. 9 (2022), 2200394, https://doi.org/10.1002/advs.202200394.

[36] H. Yang, S. Gao, D. Rao, X. Yan, Designing superior bifunctional electrocatalyst with high-purity pyrrole-type CoN_4 and adjacent metallic cobalt sites for rechargeable Zn-air batteries, Energy Stor. Mater. 46 (2022) 553–562, https://doi.org/10.1016/j.ensm.2022.01.040.

[37] F. Qiang, J. Feng, H. Wang, J. Yu, J. Shi, M. Huang, Z. Shi, S. Liu, P. Li, L. Dong, Oxygen engineering enables N-doped porous carbon nanofibers as oxygen reduction/evolution reaction electrocatalysts for flexible zinc–air batteries, ACS Catal. 12 (2022) 4002–4015, https://doi.org/10.1021/acscatal.2c00164.

[38] J. Zhang, J. Zhang, F. He, Y. Chen, J. Zhu, D. Wang, S. Mu, H.Y. Yang, Defect and doping Co-engineered non-metal nanocarbon ORR electrocatalyst, Nano-Micro Lett. 13 (2021) 65, https://doi.org/10.1007/s40820-020-00579-y.

[39] W. Wang, F. Xiong, S. Zhu, J. Chen, J. Xie, Q. An, Defect engineering in molybdenum-based electrode materials for energy storage, eScience 2 (2022) 278–294.

[40] Z. Chen, G. Zhang, Y. Wen, N. Chen, W. Chen, T. Regier, J. Dynes, Y. Zheng, S. Sun, Atomically dispersed Fe-Co bimetallic catalysts for the promoted electroreduction of carbon dioxide, Nano-Micro Lett. 14 (2021) 25, https://doi.org/10.1007/s40820-021-00746-9.

[41] Y. He, X. Yang, Y. Li, L. Liu, S. Guo, C. Shu, F. Liu, Y. Liu, Q. Tan, G. Wu, Atomically dispersed Fe–Co dual metal sites as bifunctional oxygen electrocatalysts for rechargeable and flexible Zn–air batteries, ACS Catal. 12 (2022) 1216–1227, https://doi.org/10.1021/acscatal.1c04550.

[42] Y. Xue, Y. Guo, Q. Zhang, Z. Xie, J. Wei, Z. Zhou, MOF-derived Co and Fe species loaded on N-doped carbon networks as efficient oxygen electrocatalysts for Zn-air batteries, Nano-Micro Lett. 14 (2022) 162, https://doi.org/10.1007/s40820-022-00890-w.

[43] M.-F. Qiao, Y. Wang, L. Li, G.-Z. Hu, G.-A. Zou, X. Mamat, Y.-M. Dong, X. Hu, Self-templated nitrogen-doped mesoporous carbon decorated with double transition-metal active sites for enhanced oxygen electrode catalysis, Rare Met. 39 (2020) 824–833, https://doi.org/10.1007/s12598-019-01345-9.

[44] X. Xu, J. Xie, B. Liu, R. Wang, M. Liu, J. Zhang, J. Liu, Z. Cai, J. Zou, PBA-derived FeCo alloy with core-shell structure embedded in 2D N-doped ultrathin carbon sheets as a bifunctional catalyst for rechargeable Zn-air batteries, Appl. Catal. B Environ. 316 (2022), 121687, https://doi.org/10.1016/j.apcatb.2022.121687.

[45] Y. Lei, R. Huang, H. Xie, D. Zhang, X. Liu, Y. Si, N. Li, Electronic structure tuning of FeCo nanoparticles embedded in multi-dimensional carbon matrix for enhanced bifunctional oxygen electrocatalysis, J. Alloy. Compd. 853 (2021), 157070, https://doi.org/10.1016/j.jallcom.2020.157070.

[46] W. Li, F. Wang, Z. Zhang, S. Min, Graphitic carbon layer-encapsulated Co nanoparticles embedded on porous carbonized wood as a self-supported chainmail oxygen electrode for rechargeable Zn-air batteries, Appl. Catal. B Environ. 317 (2022), 121758, https://doi.org/10.1016/j.apcatb.2022.121758.

[47] M. Wang, X. Du, M. Zhang, K. Su, Z. Li, From S-rich polyphenylene sulfide to honeycomb-like porous carbon with ultrahigh specific surface area as bifunctional electrocatalysts for rechargeable Zn-air batteries, Carbon 198 (2022) 264–274, https://doi.org/10.1016/j.carbon.2022.07.042.

[48] K. Li, R. Cheng, Q. Xue, P. Meng, T. Zhao, M. Jiang, M. Guo, H. Li, C. Fu, In-situ construction of Co/CoSe Schottky heterojunction with interfacial electron

redistribution to facilitate oxygen electrocatalysis bifunctionality for zinc-air batteries, Chem. Eng. J. 450 (2022), 137991, https://doi.org/10.1016/j.cej.2022.137991.

[49] Y. Gao, D. Zheng, Q. Li, W. Xiao, T. Ma, T. Fu, Z. Wu, L. Wang, 3D Co₃O₄-RuO₂ hollow spheres with abundant interfaces as advanced trifunctional electrocatalyst for water-splitting and flexible Zn–air battery, Adv. Funct. Mater. 32 (2022), 2203206, https://doi.org/10.1002/adfm.202203206.

[50] W. Li, J. Wang, J. Chen, K. Chen, Z. Wen, A. Huang, Core–shell carbon-based bifunctional electrocatalysts derived from COF@MOF hybrid for advanced rechargeable Zn–air batteries, Small 18 (2022), 2202018, https://doi.org/10.1002/smll.202202018.

[51] B. Zhang, T. Lu, Y. Ren, L. Huang, H. Pang, Q. Zhao, S. Tian, J. Yang, L. Xu, Y. Tang, X. Tian, Encapsulation of Co/Co₃O₄ hetero-nanoparticles within the inner tips of N-doped carbon nanotubes: engineering Mott-schottky nanoreactors for efficient bifunctional oxygen electrocatalysis toward flexible zinc-air batteries, Chem. Eng. J. 448 (2022), 137709, https://doi.org/10.1016/j.cej.2022.137709.

[52] R. Garg, L. Sahoo, K. Kaur, C.P. Vinod, U.K. Gautam, Single-step insertion of M-Nₓ moieties in commercial carbon for sustainable bifunctional electrocatalysis: mapping insertion capacity, mass loss, and carbon reconstruction, Carbon 196 (2022) 1001–1011, https://doi.org/10.1016/j.carbon.2022.06.008.

[53] M. Cao, Y. Liu, K. Sun, H. Li, X. Lin, P. Zhang, L. Zhou, A. Wang, S. Mehdi, X. Wu, J. Jiang, B. Li, Coupling Fe₃C nanoparticles and N-doping on wood-derived carbon to construct reversible cathode for Zn–air batteries, Small 18 (2022), 2202014, https://doi.org/10.1002/smll.202202014.

[54] M. Wang, L. Cao, X. Du, Y. Zhang, F. Jin, M. Zhang, Z. Li, K. Su, Highly dispersed Co-, N-, S-doped topological defect-rich hollow carbon nanoboxes as superior bifunctional oxygen electrocatalysts for rechargeable Zn–air batteries, ACS Appl. Mater. Interfaces 14 (2022) 25427–25438, https://doi.org/10.1021/acsami.2c04030.

[55] Y. Chen, S. Qiao, Y. Tang, Y. Du, D. Zhang, W. Wang, H. Zhang, X. Sun, C. Liu, Double-faced atomic-level engineering of hollow carbon nanofibers as free-standing bifunctional oxygen electrocatalysts for flexible Zn–air battery, ACS Nano 16 (2022) 15273–15285, https://doi.org/10.1021/acsnano.2c06700.

[56] W. Zhang, C.-H. Xu, H. Zheng, R. Li, K. Zhou, Oxygen-rich cobalt–nitrogen–carbon porous nanosheets for bifunctional oxygen electrocatalysis, Adv. Funct. Mater. 32 (2022), 2200763, https://doi.org/10.1002/adfm.202200763.

[57] P. Zhang, Y. Liu, S. Wang, L. Zhou, T. Liu, K. Sun, H. Cao, J. Jiang, X. Wu, B. Li, Wood-derived monolithic catalysts with the ability of activating water molecules for oxygen electrocatalysis, Small 18 (2022), 2202725, https://doi.org/10.1002/smll.202202725.

[58] J. Zhang, H. Liu, W. Zhu, B. Chen, R. Yue, S. Yin, N. Xie, R. Li, Y. Yin, Zeolitic imidazolate framework film derived CoFe-N-C nanofoams for reliable Zn-air batteries, Adv. Mater. Interfaces 10 (2023), 2201817, https://doi.org/10.1002/admi.202201817.

[59] W.Y. Noh, J. Mun, Y. Lee, E.M. Kim, Y.K. Kim, K.Y. Kim, H.Y. Jeong, J.H. Lee, H.-K. Song, G. Lee, J.S. Lee, Molecularly engineered carbon platform to anchor edge-hosted single-atomic M–N/C (M = Fe, Co, Ni, Cu) electrocatalysts of outstanding durability, ACS Catal. 12 (2022) 7994–8006, https://doi.org/10.1021/acscatal.2c00697.

[60] Y. Wang, A. Kumar, M. Ma, Y. Jia, Y. Wang, Y. Zhang, G. Zhang, X. Sun, Z. Yan, Hierarchical peony-like FeCo-NC with conductive network and highly active sites as efficient electrocatalyst for rechargeable zinc-air battery, Nano Res. 13 (2020) 1090–1099, https://doi.org/10.1007/s12274-020-2751-7.

[61] K. Ding, J. Hu, J. Luo, L. Zhao, W. Jin, Y. Liu, Z. Wu, G. Zou, H. Hou, X. Ji, Robust electronic correlation of Co-CoN₄ hybrid active sites for durable rechargeable Zn-air batteries, Adv. Funct. Mater. 32 (2022), 2207331, https://doi.org/10.1002/adfm.202207331.

[62] Z. Xu, J. Zhu, J. Shao, Y. Xia, J. Tseng, C. Jiao, G. Ren, P. Liu, G. Li, R. Chen, S. Chen, F. Huang, H.-L. Wang, Atomically dispersed cobalt in core-shell carbon nanofiber membranes as super-flexible freestanding air-electrodes for wearable Zn-air batteries, Energy Stor. Mater. 47 (2022) 365–375, https://doi.org/10.1016/j.ensm.2022.02.004.

[63] R. Wang, H. Yang, N. Lu, S. Lei, D. Jia, Z. Wang, Z. Liu, X. Wu, H. Zheng, S. Ali, F. Ma, S. Peng, Precise identification of active sites of a high bifunctional performance 3D Co/N-C catalyst in Zinc-air batteries, Chem. Eng. J. 433 (2022), 134500, https://doi.org/10.1016/j.cej.2022.134500.

[64] X. Chen, J. Pu, X. Hu, Y. Yao, Y. Dou, J. Jiang, W. Zhang, Janus hollow nanofiber with bifunctional oxygen electrocatalyst for rechargeable Zn–air battery, Small 18 (2022), 2200578, https://doi.org/10.1002/smll.202200578.

[65] W.-W. Tian, J.-T. Ren, Z.-Y. Yuan, In-situ cobalt-nickel alloy catalyzed nitrogen-doped carbon nanotube arrays as superior freestanding air electrodes for flexible zinc-air and aluminum-air batteries, Appl. Catal. B Environ. 317 (2022) 121764, https://doi.org/10.1016/j.apcatb.2022.121764.

[66] P. Du, K. Hu, J. Lyu, H. Li, X. Lin, G. Xie, X. Liu, Y. Ito, H.-J. Qiu, Anchoring Mo single atoms/clusters and N on edge-rich nanoporous holey graphene as bifunctional air electrode in Zn–air batteries, Appl. Catal. B Environ. 276 (2020) 119172, https://doi.org/10.1016/j.apcatb.2020.119172.

[67] J. Li, Y. Kang, Z. Lei, P. Liu, Well-controlled 3D flower-like CoP₃/CeO₂/C heterostructures as bifunctional oxygen electrocatalysts for rechargeable Zn-air batteries, Appl. Catal. B Environ. 321 (2023), 122029, https://doi.org/10.1016/j.apcatb.2022.122029.

[68] C. Zhang, C. Wu, Y. Gao, Y. Gong, H. Liu, J. He, FeNi nanoparticles coated on N-doped ultrathin graphene-like nanosheets as stable bifunctional catalyst for Zn-air batteries, Chem. Asian J. 16 (2021) 1592–1602, https://doi.org/10.1002/asia.202100347.

[69] O. Yadorao Bisen, A. Kumar Yadav, B. Pavithra, K. Kar Nanda, Electronic structure modulation of molybdenum-iron double-atom catalyst for bifunctional oxygen electrochemistry, Chem. Eng. J. 449 (2022), 137705, https://doi.org/10.1016/j.cej.2022.137705.

[70] Y. Zhang, Z. Zhang, G. Jiang, A.H. Mamaghani, S. Sy, R. Gao, Y. Jiang, Y. Deng, Z. Bai, L. Yang, A. Yu, Z. Chen, Three-dimensionally ordered mesoporous Co₃O₄ decorated with Mg as bifunctional oxygen electrocatalysts for high-performance zinc-air batteries, Nano Energy 100 (2022), 107425, https://doi.org/10.1016/j.nanoen.2022.107425.

[71] Y. Pan, S. Liu, K. Sun, X. Chen, B. Wang, K. Wu, X. Cao, W.-C. Cheong, R. Shen, A. Han, Z. Chen, L. Zheng, J. Luo, Y. Lin, Y. Liu, D. Wang, Q. Peng, Q. Zhang, C. Chen, Y. Li, A Bimetallic Zn/Fe polyphthalocyanine-derived single-atom Fe-N₄ catalytic site: a superior trifunctional catalyst for overall water splitting and Zn–air, Batter. Angew. Chem. Int. Ed. 57 (2018) 8614–8618, https://doi.org/10.1002/anie.201804349.

[72] Y. Deng, J. Zheng, B. Liu, H. Li, M. Yang, Z. Wang, Schiff-base polymer derived FeCo-N-doped porous carbon flowers as bifunctional oxygen electrocatalyst for long-life rechargeable zinc-air batteries, J. Energy Chem. 76 (2023) 470–478, https://doi.org/10.1016/j.jechem.2022.09.031.

[73] Z. Peng, S. Yang, D. Jia, P. Da, P. He, A.M. Al-Enizi, G. Ding, X. Xie, G. Zheng, Homologous metal-free electrocatalysts grown on three-dimensional carbon networks for overall water splitting in acidic and alkaline media, J. Mater. Chem. A 4 (2016) 12878–12883, https://doi.org/10.1039/C6TA04426C.

[74] J.-M. Ju, C.H. Lee, J.H. Park, J.-H. Lee, H. Lee, J.-H. Shin, S.-Y. Kwak, S.U. Lee, J.-H. Kim, Structural and electronic modulations of imidazolium covalent organic framework-derived electrocatalysts for oxygen redox reactions in rechargeable Zn–air batteries, ACS Appl. Mater. Interfaces 14 (2022) 24404–24414, https://doi.org/10.1021/acsami.2c04194.

[75] Y. Liu, Z. Chen, Z. Li, N. Zhao, Y. Xie, Y. Du, J. Xuan, D. Xiong, J. Zhou, L. Cai, Y. Yang, CoNi nanoalloy-Co-N₄ composite active sites embedded in hierarchical porous carbon as bi-functional catalysts for flexible Zn-air battery, Nano Energy 99 (2022), 107325, https://doi.org/10.1016/j.nanoen.2022.107325.

[76] W. Wan, C.A. Triana, J. Lan, J. Li, C.S. Allen, Y. Zhao, M. Iannuzzi, G.R. Patzke, Bifunctional single atom electrocatalysts: coordination–performance correlations and reaction pathways, ACS Nano 14 (2020) 13279–13293, https://doi.org/10.1021/acsnano.0c05088.

[77] S. Ren, X. Duan, F. Ge, Z. Chen, Q. Yang, M. Zhang, H. Zheng, Novel MOF-derived hollow CoFe alloy coupled with N-doped ketjen black as boosted bifunctional oxygen catalysts for Zn–air batteries, Chem. Eng. J. 427 (2022), 131614, https://doi.org/10.1016/j.cej.2021.131614.

[78] H. Liu, Y. Liu, S. Mehdi, X. Wu, T. Liu, B. Zhou, P. Zhang, J. Jiang, B. Li, Surface phosphorus-induced CoO coupling to monolithic carbon for efficient air electrode of quasi-solid-state Zn–air batteries, Adv. Sci. 8 (2021), 2101314, https://doi.org/10.1002/advs.202101314.

[79] L. Zhang, Y. Zhu, Z. Nie, Z. Li, Y. Ye, L. Li, J. Hong, Z. Bi, Y. Zhou, G. Hu, Co/MoC nanoparticles embedded in carbon nanoboxes as robust trifunctional electrocatalysts for a Zn–air battery and water electrocatalysis, ACS Nano 15 (2021) 13399–13414, https://doi.org/10.1021/acsnano.1c03766.

[80] M. Yi, N. Li, B. Lu, L. Li, Z. Zhu, J. Zhang, Single-atom Pt decorated in heteroatom (N, B, and F)-doped ReS₂ grown on Mo₂CTₓ for efficient pH-universal hydrogen evolution reaction and flexible Zn–air batteries, Energy Stor. Mater 42 (2021) 418–429, https://doi.org/10.1016/j.ensm.2021.07.048.

[81] Y.-P. Chen, S.-Y. Lin, R.-M. Sun, A.-J. Wang, L. Zhang, X. Ma, J.-J. Feng, FeCo/FeCoP encapsulated in N, Mn-codoped three-dimensional fluffy porous carbon nanostructures as highly efficient bifunctional electrocatalyst with multi-components synergistic catalysis for ultra-stable rechargeable Zn-air batteries, J. Colloid Interface Sci. 605 (2022) 451–462, https://doi.org/10.1016/j.jcis.2021.07.082.

[82] J.-C. Li, Y. Meng, L. Zhang, G. Li, Z. Shi, P.-X. Hou, C. Liu, H.-M. Cheng, M. Shao, Dual-phasic carbon with Co single atoms and nanoparticles as a bifunctional oxygen electrocatalyst for rechargeable Zn–air batteries, Adv. Funct. Mater. 31 (2021), 2103360, https://doi.org/10.1002/adfm.202103360.

[83] K. Min, K. Sim, E. Lee, G. Yoo, H.C. Ham, S.E. Shim, D. Lim, S.-H. Baeck, A hierarchical Co₃O₄/CoS microbox heterostructure as a highly efficient bifunctional electrocatalyst for rechargeable Zn–air batteries, J. Mater. Chem. A 9 (2021) 17344–17352, https://doi.org/10.1039/D1TA01912K.

[84] J.-T. Ren, Y.-D. Ying, Y.-P. Liu, W. Li, Z.-Y. Yuan, Charge redistribution caused by sulfur doping of bimetal FeCo phosphides supported on heteroatoms-doped graphene for Zn-air batteries with stable cycling, J. Energy Chem. 71 (2022) 619–630, https://doi.org/10.1016/j.jechem.2022.03.048.

[85] P. Thangasamy, S. Oh, H. Randriamahazaka, S. Nam, I.-K. Oh, Mechanistic insight into collectively exhaustive CoPi-NPC nanosheets for oxygen reduction reaction and Zn-air battery, Appl. Catal. B Environ. 316 (2022), 121656, https://doi.org/10.1016/j.apcatb.2022.121656.

[86] Y.-W. Li, W.-J. Zhang, J. Li, H.-Y. Ma, H.-M. Du, D.-C. Li, S.-N. Wang, J.-S. Zhao, J.-M. Dou, L. Xu, Fe-MOF-derived efficient ORR/OER bifunctional electrocatalyst for rechargeable zinc-air batteries, ACS Appl. Mater. Interfaces 12 (2020) 44710–44719, https://doi.org/10.1021/acsami.0c11945.

[87] K. Kim, K. Min, Y. Go, Y. Lee, S.E. Shim, D. Lim, S.-H. Baeck, FeCo alloy nanoparticles embedded in N-doped carbon supported on highly defective ketjenblack as effective bifunctional electrocatalysts for rechargeable Zn–air batteries, Appl. Catal. B Environ. 315 (2022), 121501, https://doi.org/10.1016/j.apcatb.2022.121501.

[88] J. Yu, Y. Dai, Z. Zhang, T. Liu, S. Zhao, C. Cheng, P. Tan, Z. Shao, M. Ni, Tailoring structural properties of carbon via implanting optimal Co nanoparticles in N-rich carbon cages toward high-efficiency oxygen electrocatalysis for rechargeable Zn-

air batteries, Carbon Energy 4 (2022) 576–585, https://doi.org/10.1002/cey2.171.

[89] X. Duan, S. Ren, N. Pan, M. Zhang, H. Zheng, MOF-derived Fe,Co@N–C bifunctional oxygen electrocatalysts for Zn–air batteries, J. Mater. Chem. A 8 (2020) 9355–9363, https://doi.org/10.1039/D0TA02825H.

[90] K. Wu, L. Zhang, Y. Yuan, L. Zhong, Z. Chen, X. Chi, H. Lu, Z. Chen, R. Zou, T. Li, C. Jiang, Y. Chen, X. Peng, J. Lu, An Iron-decorated carbon aerogel for rechargeable flow and flexible Zn–air batteries, Adv. Mater. 32 (2020), 2002292, https://doi.org/10.1002/adma.202002292.